International Journal of Pharmaceutics 455 (2013) 338–347

Contents lists available at ScienceDirect

International Journal of Pharmaceutics

journal homepage: www.elsevier.com/locate/ijpharm

Pharmaceutical nanotechnology

The design trend in tissue-engineering scaffolds based on nanomechanical properties of individual electrospun nanofibers

Biljana Janković[a,*], Jan Pelipenko[a], Miha Škarabot[b], Igor Muševič[b], Julijana Kristl[a]

[a] University of Ljubljana, Faculty of Pharmacy, Ljubljana, Slovenia
[b] Jožef Stefan Institute, Department of Condensed Matter Physics, Ljubljana, Slovenia

ARTICLE INFO

Article history:
Received 27 March 2013
Received in revised form 26 June 2013
Accepted 30 June 2013
Available online 29 July 2013

Keywords:
Electrospinning
Nanofiber
Atomic force microscopy
Tissue engineering
Elasticity

ABSTRACT

This paper especially highlights the finding that the mechanical properties of polymeric nanofibers can be tuned by changing the fiber size as well as the composition. For this purpose, the bending Young's modulus was determined using atomic force microscope by involving single-material (polyvinyl alcohol (PVA), polyethylene oxide (PEO 400K)) and composite nanofibers (polyvinyl alcohol/hyaluronic acid (PVA/HA), polyethylene oxide/chitosan (PEO 400K/CS)). The mechanical property, namely the bending Young's modulus, increases as the diameter of the fibers decreases from the bulk down to the nanometer regime (less than 200 nm). The ranking of increasing stiffness according to the AFM measurements of the three-point beam bending test are in agreement, and can be ranked: PEO 400K < PVA/HA ≈ PVA < PEO < 400K/CS. According to our results, CS-based nanofibers are the stiffest (15 GPa) and the most resilient to erosion in an aqueous medium. Consequently, they possess the most appropriate attributes for bone, tendon, and cartilage tissue scaffold engineering. Nanofibers based on PVA (6 GPa) and PEO (3 GPa) are more elastic (a smaller bending Young's modulus) and therefore are the most suitable for skin and wound tissue scaffolds.

© 2013 Elsevier B.V. All rights reserved.

1. Introduction

It is generally accepted that electrospinning has the potential to fabricate scaffolds as it results in a material with sufficient strength, nanostructure, biocompatibility, and economic attractiveness (Rošic et al., 2012, 2011; Jin et al., 2012; Inai et al., 2005; Li et al., 2005). A scaffold design based on nanofibers can successfully mimic the structure and components of extracellular matrix (ECM) components in the body and therefore properties of other native tissues (Yim and Leong, 2005; Stitzel et al., 2001). Specifically, the ECM consists of a cross-linked network of collagen and elastin fibrils (mechanical framework), interspersed with glycosaminoglycans (biochemical interactions). In spite of its remarkable diversity due to the presence of various biomacromolecules and their organization, a key feature of native ECM is the nanoscale dimension of its internal components. Moreover, structural proteins such as collagen and elastin fibrils have diameters ranging from 10 to several hundred nanometers and are twisted together in order to form a nonwoven network, which is responsible for the sufficient tensile strength and elasticity of the tissue (Fleming et al., 1999). Other fundamental features are the pores, ridges, and grooves of the ECM basement membrane, which are also nanoscaled (Johnson et al., 2007; Fleming et al., 1999). Compounding this, processing biocompatible polymers into nanofibers and networks represents the initial step toward mimicking some aspects of native ECM structure from at least the mechanical and biological perspectives (Rim et al., 2013). In view of the correlations between the structural integrity of scaffolds and cell growth and differentiations, there is a need to investigate the mechanical properties of single nanofibers as the basic construct elements of the scaffolds (Ji et al., 2012). One of the direct implications for characterizing the fiber is the closest estimation of what cells actually experience in their surroundings. Furthermore, assessment of the nanomechanical attributes of individual nanofibers may also facilitate the properties of the resulting scaffold and offer insight into size-dependent mechanical behavior of the polymeric nanofibers (Johnson et al., 2007; Tan and Lim, 2006a). In this study, we compare the mechanical properties of single-material electrospun polyvinyl alcohol (PVA), polyethylene oxide (PEO), and composite nanofibers. Namely, for the manufacturing purposes of composite nanofibers, synthetic polymers such as PVA and PEO have been utilized to form a fibrous backbone, whereas natural polymers such as chitosan (CS) and hyaluronic acid (HA) act as promoters for cell attachment to the scaffold and facilitate their growth. PVA and PEO are water-soluble and biodegradable polymers, which have largely been employed in the

* Corresponding author at: Aškerčeva 7, 1000 Ljubljana, Slovenia.
Tel.: +386 1 476 9617; fax: +386 1 425 8031.
E-mail address: biljana.jankovic@ffa.uni-lj.si (B. Janković).

0378-5173/$ – see front matter © 2013 Elsevier B.V. All rights reserved.
http://dx.doi.org/10.1016/j.ijpharm.2013.06.083

Table 1
Processing conditions for electrospinning nanofibers.

Polymer solution	Flow rate (ml/h)	Tip distance (cm)	Voltage (kV)
PVA	0.7	15	15
PVA/HA	1.6	18.5	25
PEO 400K	1.8	17	20
PEO 400K/CS	1.8	17	25

pharmaceutical industry due to their biocompatibility. They also express high self-crosslink capability and charge-carrying capacity, which are essential for the electrospinning process (Fu et al., 2010). On the other hand, CS is a favorable polymer option for tissue engineers because it can reinforce the mechanical integrity of the scaffolds and it shows excellent cell adhesive properties due to the presence of amine groups (Martins et al., 2010; Zhang et al., 2008; Subramanian et al., 2005). HA is an appropriate candidate for a tissue-engineering scaffold matrix because it is a native component of ECM, is environmentally sustainable, and is a non-immunogenic polymer that plays a vital role in wound-healing processes (Du et al., 2011).

The objective of this study was to evaluate the morphology, mechanical properties, and thermal and swelling behavior of prepared single electrospun nanofibers with respect to their variations in the composition and size. For the purposes of local and bulk compositional analysis, the following methods were conducted: atomic force microscopy (AFM), differential scanning calorimetry (DSC), and attenuated total reflectance spectroscopy (ATR). The measurements presented in this paper were conducted on the optimized nanofibers regarding the process parameters and their composition, which have recently been reported in our works (Rošic et al., 2012; Pelipenko et al., 2013; Rošic et al., 2013). This paper especially highlights the finding that the mechanical properties of polymeric nanofibers can be tuned by changing the fiber size as well as the composition. Therefore, our ultimate goal was to assign the mechanical properties of single-material and composite nanofibers in order to match the mechanical properties of native tissues. According to the assessed mechanical properties, the nanofibers will be categorized for the specific tissue scaffold applications.

2. Materials and methods

2.1. Materials

PVA (MW 125,000 g/mol), HA sodium salt from *Streptococcus equi*, PEO (MW 400,000 g/mol), CS (low viscous), and Triton® X-100 were supplied by Sigma–Aldrich (St. Louis, MO, USA). Glacial acetic acid and DMSO (purity ≥ 99.9%) and glutaraldehyde (50% solution in water) were provided from Merck (Darmstadt, Germany), and ethanol (96%) from Kefo (Ljubljana, Slovenia).

2.2. Preparation of nanofibers – electrospinning

A blended solution of PVA and HA was prepared by combining PVA and HA in 80:20 mass ratio. Final polymer concentration was 5% (w/w). Subsequently, ethanol, glutaraldehyde and Triton X-100 were added in concentrations 6.4% (v/v), 0.2% (v/v) and 1.3% (v/v), respectively, in order to improve nanofiber stability and solution spinnability. The final solution was stirred on a magnetic stirrer for 24 h. A 3% (w/w) PEO solution was prepared by dissolving PEO 400K in distilled water, and a blended solution of PEO and CS was prepared by mixing 3% (w/w) CS solution in 2% (w/w) acetic acid in a mass ratio of 90:10. The final composition was stirred for 24 h on a magnetic stirrer.

Table 1 summarizes the processing conditions for all the electrospun fibers in this study. For each set of fibers, the flow rate was set between 0.7 and 1.8 ml/h and the electrical voltage between 15 kV and 25 kV. The distance between the needle tip and collector was adjusted from 15 cm to 18.5 cm. In addition, PVA nanofibers were thermally stabilized at 160 °C for 30 min.

2.3. Thermal analysis of nanofibers studied

Thermal analysis was carried out to measure the melting and crystallization behavior of nanofibers studied with a DSC1 Mettler-Toledo instrument (Columbus, OH, USA). The analysis parameters were followed: sample weight ~ 5 mg, placed in a covered, pierced aluminum pan, heating rate 10 °C/min in a temperature interval from 25 to 340 °C/min under a nitrogen purge (30 ml/min). The DSC temperature and heat flow values were calibrated with indium as standard.

2.4. Attenuated total reflectance infrared spectroscopy (ATR-IR) of nanofibers studied

The ATR-IR spectra of the pure components and nanofibers studied were obtained with a Thermo Nicolet Nexus instrument (Thermo Fisher Scientific, Waltham, MA, USA) with an ATR DuraSamplIR attachment (Smiths Detection Group). Spectra were recorded between 4000 and 500 cm^{-1} through the accumulation of 1000 scans with a resolution of 8 cm^{-1}.

2.5. Morphological observation of the nanofibers with AFM

For morphological characterization and the determination of the average fiber diameter, the groups of samples studied were electrospun on cover glass. Contact-mode AFM images of nanofiber morphology in a dry state were acquired with a Nanoscope IIIa multimode scanning probe microscope equipped with an E-type scanner (Veeco, Santa Barbara, CA, USA). Sharp silicone probes (MSCT, Veeco, Santa Barbara, CA, USA) with a nominal spring constant of 0.1 N/m were used for imaging. Data were recorded at a scan rate of 3.0 Hz and stored in a 512 × 512 pixel format. The images obtained were processed using the Nanoscope software. For size distribution purposes, at least 50 fibers were taken into consideration.

2.6. Polymeric phase behavior of nanofibers

The structures and the polymeric phase separation of the groups of nanofibers were determined with the phase imaging mode of AFM (AFM 5500, Agilent, Santa Clara, CA, USA) after fiber deposition on the cover slips. Phase imaging was also used as a complementary technique for mapping variations of nanofiber elasticity. Harder parts of material or regions with enhanced repulsive interactions appear as bright, whereas softer or adhesive areas show up as darker regions in the images. The origin for this lies in the larger phase lag of the cantilever oscillation on softer regions during the tip scanning in comparison to stiffer regions.

2.7. Measurement of the nanofibers elastic properties with AFM

The elastic properties of electrospun nanofibers were studied with an AFM Nanoscope IIIa Multimode (Digital Instruments, Santa Barbara, CA, USA) and silicon cantilever with a nominal spring constant 0.58 N/m (SLN, Bruker, Santa Barbara, CA, USA) by performing the nanoscale three-point bending test. As a substrate we utilized an AFM calibration grating (TGZ03, step height range 500 ± 5 nm, pitch 3 μm, Mikromasch, San Jose, CA, USA). During electrospinning, the nanofibers were randomly oriented on the

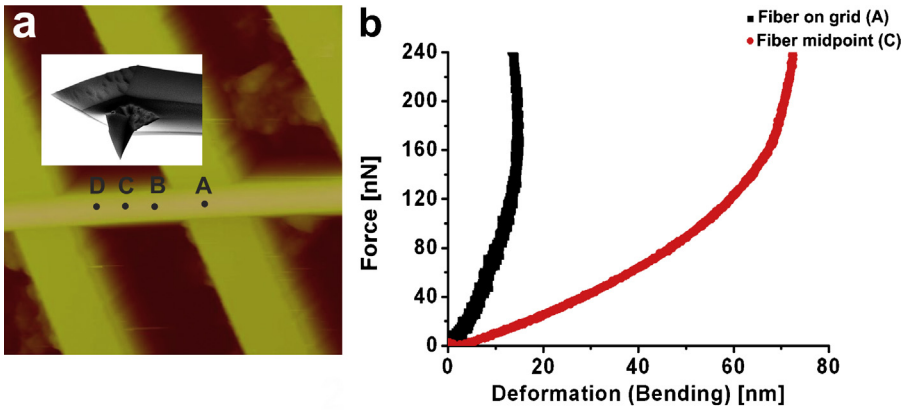

Fig. 1. (a) AFM height image of a single PVA nanofiber positioned over the grooves of the AFM grid; (b) force-deformation (bending) curves obtained at the fiber midpoint (C) and fiber on the grid (A). B and D are the control points from the fiber midpoint.

AFM grid, and thus only fibers perpendicular to the groove were selected for the measurements. In such cases we applied a force with the AFM tip at different positions along the nanofiber and measured the deflection (Fig. 1a).

Deflection measured on the supported nanofiber with the substrate (Point A – Fig. 1a) was subtracted from the deflection measured at the middle point (Point C – Fig. 1a). In this manner, we compensated for the penetration of the AFM tip into the nanofiber. To check the reliability of the midpoint test, two extra measurements along the fibers were conducted (Points B, D – Fig. 1a). For the purposes of particular measurements, at least six nanofibers were tested to determine the bending elastic modulus.

Here we would like to repeat the assumptions and calculations concerned in the proposed three-point bending method (Humar et al., 2006; Salvetat et al., 1999). The nanofiber is assumed to be a prismatic elastic beam with both ends fixed, which experiences pure deflection as force is applied (shear deformation is negligible). The adhesion between the fiber and substrate was sufficiently strong because both fiber ends were found to remain in place after the test was conducted. For the further calculations, we assumed that variations of nanofiber dimensions along the length were negligible. Consequently, average height and width measured on the fiber portions lying on the silicon groove were taken to be representative proportions of the nanofibers. The bending Young's modulus (E) of the nanofibers studied can be calculated using the following equation:

$$E = \frac{FL^3}{192I\delta} \tag{1}$$

where F represents the applied force, I is the moment of inertia, and L is the nanofiber length over the groove, δ is the deformation. After the deposition to the AFM grid, the nanofibers assumed an elliptical shape, and thus I can be determined as:

$$I = \frac{\pi ab^3}{4} \tag{2}$$

where a and b are the long and short axes of the ellipse, respectively.

2.8. Nanoindentation of polymeric films

In order to compare mechanical properties at the single fiber and bulk level, nanomechanical characterization of polymeric films in the same composition were conducted. Polymeric films were prepared using a solution casting method. Four grams of each polymer solution were poured into a round mold with a diameter of 4 cm and left to dry at room atmosphere ($T = 22 \pm 1\,^{\circ}$C, RH = 33%) for 1 week.

In the individual experiments, nanoindentation was performed at room temperature using an Agilent G200 nanoindenter (Agilent, Santa Clara, CA, USA), equipped with a CSM (continuous stiffness measurement) module. A three-sided pyramidal Berkovich indenter was utilized to determine the mechanical properties of the polymeric films studied. Thermal drifts were ensured to be consistently low (typically <0.05 nm/s). Moreover, nanoindentation experiments were conducted under dynamic displacement-controlled CSM mode (2000 nm), and thus E and indentation hardness (H) can be obtained as a function of indentation depth. This was attained by superimposing a 2 nm sinusoidal displacement at 45 Hz onto the primary loading signal, while tracking the system response *via* a frequency-specific amplifier. The loading and unloading strain rate targets were set at 0.05 s^{-1}. At the maximum displacement (2000 nm), the indenter was held for 15 s prior to unloading in order to minimize creep effects. A total number of 30 indentations were performed on each polymeric film.

According to the dynamic CSM mode, E can be determined as a function of the surface penetration depth (h). This is accomplished by continuously monitoring the alteration in the elastic contact stiffness (S), which was further applied to calculate the reduced modulus (E_r):

$$E_r = \frac{\sqrt{\pi}}{2\beta}\frac{S}{\sqrt{A_c}} \tag{3}$$

where A_c is the projected contact area, and β is a constant that depends on the indenter's geometry ($\beta = 1.034$ for Berkovich tip).

Referring to Oliver and Pharr's theory (Oliver and Pharr, 2004), the elastic modulus can be extracted from the following equation:

$$\frac{1}{E_r} = \left(\frac{1-\nu_s^2}{E}\right) + \left(\frac{1-\nu_i^2}{E_i}\right) \tag{4}$$

where E_i and ν_i represent the elastic modulus and Poisson's ratio of the indenter (for the diamond tip: $E_i = 1141$ GPa and $\nu_i = 0.07$). For the purposes of our experiments, all elastic moduli were calculated using Poisson's ratio of the sample (ν_s) as 0.3.

The indentation hardness, H, is calculated as the ratio between the applied load (P) and projected contact area (A_c):

$$H = \frac{P}{A_c} \tag{5}$$

The projected contact area (A_c) is derived from the contact depth (h_c) according to the following equation:

$$h_c = h_{max} - 0.75\left(\frac{P}{S}\right) \tag{6}$$

Table 2
Melting points (T_m) and enthalpies of fusion (ΔH) for pure components and nanofibers studied.

Sample	T_m (°C)	ΔH (J/g)
PVA powder	221	−64.7
PVA nanofibers	229	−55.4
PVA/HA nanofibers	218	−38.2
PEO 400K powder	64	−230.6
PEO 400K nanofibers	61	−179.5
PEO 400K/CS nanofibers	69	−124.41

where h_{max} is the maximum indentation depth, and 0.75(P/S) expresses the extent of elastic recovery.

2.9. Swelling and erosion of electrospun nanofibers

Depending upon application, the structural integrity of the electrospun nanofibers should be studied keeping in mind the surrounding environment of the scaffolds once placed in an *in vivo* system. From another point of view, as the scaffold degrades it is substituted with natural tissue. If the degradation rate of nanofibers is faster than tissue regeneration, the scaffolds will lose their support function for tissue growth.

The groups of nanofibers studied were deposited on cover slips and subjected to a swelling study in the fluid cell on AFM over 60 min. Briefly, the liquid cell was positioned on the cover slip, and AFM imaging in distilled water was performed using a liquid imaging cell sealed with an O-ring. The morphology of nanofibers after water immersion was characterized by a Nanoscope IIIa multimode scanning probe microscope equipped with an E-type scanner (Veeco, Santa Barbara, CA, USA). Silicon nitride cantilevers (MSCT, Veeco, Santa Barbara, CA, USA) with a spring constant of 0.1 N/m were used for imaging. Data were recorded at a scan rate of 3 Hz and stored in a 512 × 512 pixel format. The heights of the individual swollen nanofibers in water were determined from the cross-sectional analysis on AFM images after 5, 10, 15, 20, 30, 45, and 60 min. The % of swelling was calculated in comparison to average fiber height in the dry state according to Eq. (7):

$$\%\,\text{of swelling} = \frac{h_1 - h_0}{h_0} \quad (7)$$

where h_1 is the height of the swelled fiber and h_0 is the average height of the dry fiber.

The swelling behavior of each group studied was estimated on at least 10 individual nanofibers.

3. Results and discussion

3.1. Thermal behavior of nanofibers

In order to investigate thermal behavior, such as melting and the formation of crystalline structure, DSC measurements were performed on pure powdered components as well as the investigated nanofibers. The DSC results and the calculated parameters are presented in Fig. 2 and Table 2.

The endothermic peaks during the heating stage, centered in a range from 218 to 229 °C, are attributed to the melting point of the crystalline PVA phase (Fig. 2a). The broad endothermic peak in the PVA nanofibers curve is attributed to the evaporation of bound water (Fig. 2a). This effect is well explained in the literature (Peresin et al., 2010). The melting temperature in the electrospun PVA nanofibers is slightly shifted to higher values. The annealing of the PVA nanofibers can be the reason for increasing of crystals order degree (alignment and enhanced crystallization of the polymer chains within the individual PVA fibers) or decreasing of the crystals defects. This can be the reason for elevation of melting temperature. The results are in accordance with the literature data (Peresin et al., 2010).

On the other hand, after adding the HA, the melting temperature of the PVA/HA nanofibers is repositioned to a lower value (Table 2). In both cases, the melting enthalpy decreased with the process of electrospinning, whereas the reduction is even more emphasized by the incorporation of the HA (Table 2). Such results suggest that the perfection of the molecular orientation is diminished by HA loading and the electrospinning process as well.

The reduction of crystallinity (ordered structure) after electrospinning can be easily explained by the fact that the jet ejected from a capillary under the strong electrostatic potential experiences an extensive elongational flow to stretch the polymer chains in the electrostatic field direction. At the same time, the solvent evaporates within a very short period of time. As a result, solidification of the electrospun jet occurs rapidly, which contributes to decreasing the molecular ordering (crystallinity) and T_m (Garg and Bowlin, 2011).

The more emphasized reduction of the ΔH for the PVA/HA nanofibers imply possible interactions; that is, hydrogen bonding between these polymers. It is possible that the altered thermal properties are consistent with the previously reported literature data and are related to the increased number of OH groups in the HA polymer (Kim et al., 2011).

The DSC curve of PEO 400K powder (Fig. 2b) shows only one endothermic event with its maximum at approximately 64 °C, related to the crystalline melt of pure PEO. Increased anisotropy of PEO 400K nanofibers can be additionally confirmed according to reduced ΔH in comparison to pure powder.

The broad endothermic peak in the CS curve is attributed to the evaporation of bound water (Fig. 2b). The DSC thermograms of composite nanofiber PEO 400K/CS exhibited one endothermic event, which demonstrated its maximum intensity at the temperature of PEO melting. In both cases, the T_m and ΔH (isotropy) are decreased in comparison to pure PEO powder. This significant reduction of ΔH is not in agreement with the weight fraction of CS in the nanofibers, which implies possible hydrogen bond formation between the ether groups of PEO and amino groups of CS (Martinova and Lubasova, 2008).

3.2. Structural changes of nanofibers upon electrospinning: ATR study

ATR spectroscopy was performed to determine any structural changes of polymeric chains upon electrospinning as well as the interactions between PVA and HA, and between PEO and CS (Fig. 3). Typical assignments of ATR spectra of the pure PVA powder are represented in Table S1 – Supporting Information. The electrospun PVA nanofibers demonstrated spectral features similar to the PVA powder, although some minor changes in their relative intensities and peak positions can be noticed. The large bands observed between 3400 and 3200 cm^{-1} were typical for the stretching of OH group due to the intermolecular and intramolecular hydrogen bonds. The vibrational band observed between 2940 and 2900 cm^{-1} corresponded to the stretching C—H from the alkyl groups. The symmetric stretching band shifted to a higher value at 2908 from 2903 cm^{-1} in case of PVA nanofibers. The most significant alteration can be reported for C—C stretching at the 1139 cm^{-1} band. This result implies reduction of PVA crystallinity upon electrospinning, which is in agreement with the DSC measurements (decreased ΔH).

After HA was incorporated into PVA nanofibers, the prevailing broad absorption band associated with the bending of the OH groups (1416 cm^{-1}) shifts to a higher wave number region (1440 cm^{-1}). This result implies stronger hydrogen bonding in PVA/HA nanofibers due to the increase in the number of OH groups

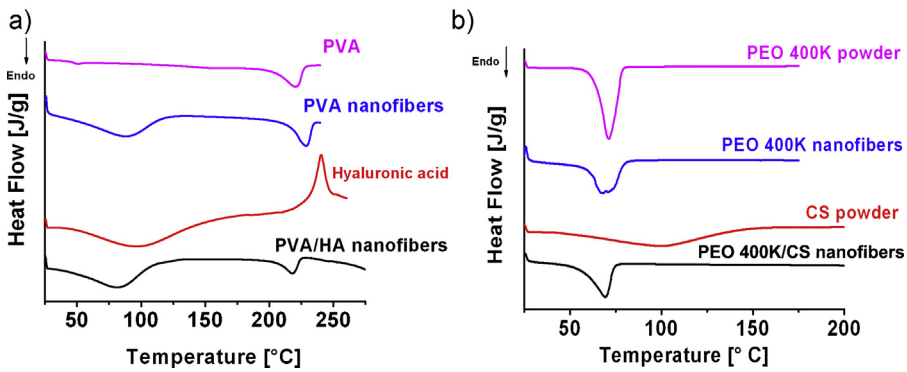

Fig. 2. DSC thermograms of pure components and nanofibers studied.

by adding the HA. Such a result is consistent with the observation made from the DSC measurements (decreased ΔH, Table 2).

Typical ATR spectra of the PEO 400K/CS and PEO 400K nanofibers as well as of their pure components are shown in Fig. 3b. The vibration bands of amino (1583 cm^{-1}), amide (1658 cm^{-1}), and hydroxyl (3354 cm^{-1}) groups of CS were shifted to 1575 cm^{-1}, 1648 cm^{-1}, and 3404 cm^{-1} (Table S2 – Supporting Information). Such results indicated specific interaction between ether groups of PEO and amino, amide, and hydroxyl groups of CS, which is in agreement with the DSC measurements (decreased ΔH, Table 2).

3.3. Morphology and diameters of electrospun nanofibers

The morphologies and distributions of electrospun nanofibers heights are presented in Fig. 4. AFM evaluation revealed the formation of solid nanofibers with non-porous surfaces and a random orientation. Analysis of fiber height with the AFM cross-sectional analysis revealed a distribution of sizes, which is common for the electrospun nanofibers. We noticed that their cross-section could not simply be considered a circular shape. This can be connected with the manner of the fiber's collection and insufficiently fast rate of drying because its contact with the cover glass promoted its broadening and the formation of nanofibers with an elliptical cross-section.

Since the distributions of the sizes were not normal in the most cases, median values for the nanofibers heights were calculated. In that manner, the ranking of the increasing nanofibers height according to the median values can be ranked: PEO 400K (97.5 nm) < PVA/HA (159.3 nm) < PEO 400K/CS (270 nm) < PVA (279.7 nm).

3.4. Polymeric phase behavior of nanofibers

The phase image of PVA nanofibers reveals a filamentous structure with alternating crystalline and amorphous regions within each fibril (Fig. 5a). Such a fibrous structure is related to the drawing process of electrospinning, which orients the polymer molecules in the direction of the fiber's axis (Zussman et al., 2003; Buchko et al., 1999). Even more pronounced homogeneous thread-like structure was observed in the case of PEO 400K nanofibers (Fig. 5c).

On the other hand, PVA/HA nanofibers demonstrate more nanogranular morphology, whereas some fibrils still appear to exist (Fig. 5b). Evidently, nanofibers with the granular morphology are thinner (Fig. 4b) because the crystallites are more densely packed.

The presence of the separated phases in the case of composite nanofibers can be additionally visualized using AFM phase imaging. Phase separation can induce variation in the mechanical properties and thus can be undesirable. The phase images of PVA/HA and single-material nanofibers do not show a strong contrast between the different domains, which indicates the homogenous structure of the samples studied (Fig. 5a and b). However, when the CS was blended with PEO 400K, a moderate contrast (sudden change in intensity) was observed. This is also apparent from the intensity plot, where a certain decrease in phase was noticed. Because a chemical interaction between the CS and PEO was determined with the DSC and ATR (Fig. 3, S2 - Supporting information), phase separation due to the immiscibility of the polymers is diminished. Therefore, differences in their mechanical properties or the surface defects (surface depression) could be the possible reason for the phase intensity change.

Finally, phase images can be used to map the variations in surface properties such as elasticity, which is based on the interaction

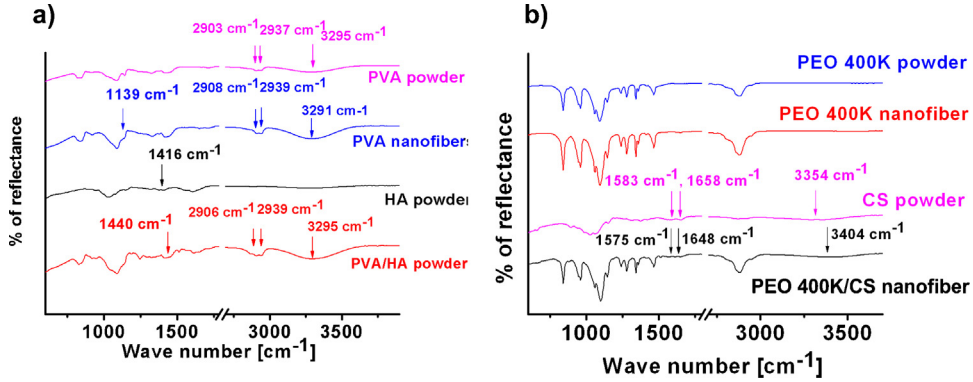

Fig. 3. ATR spectra of pure components and nanofibers studied.

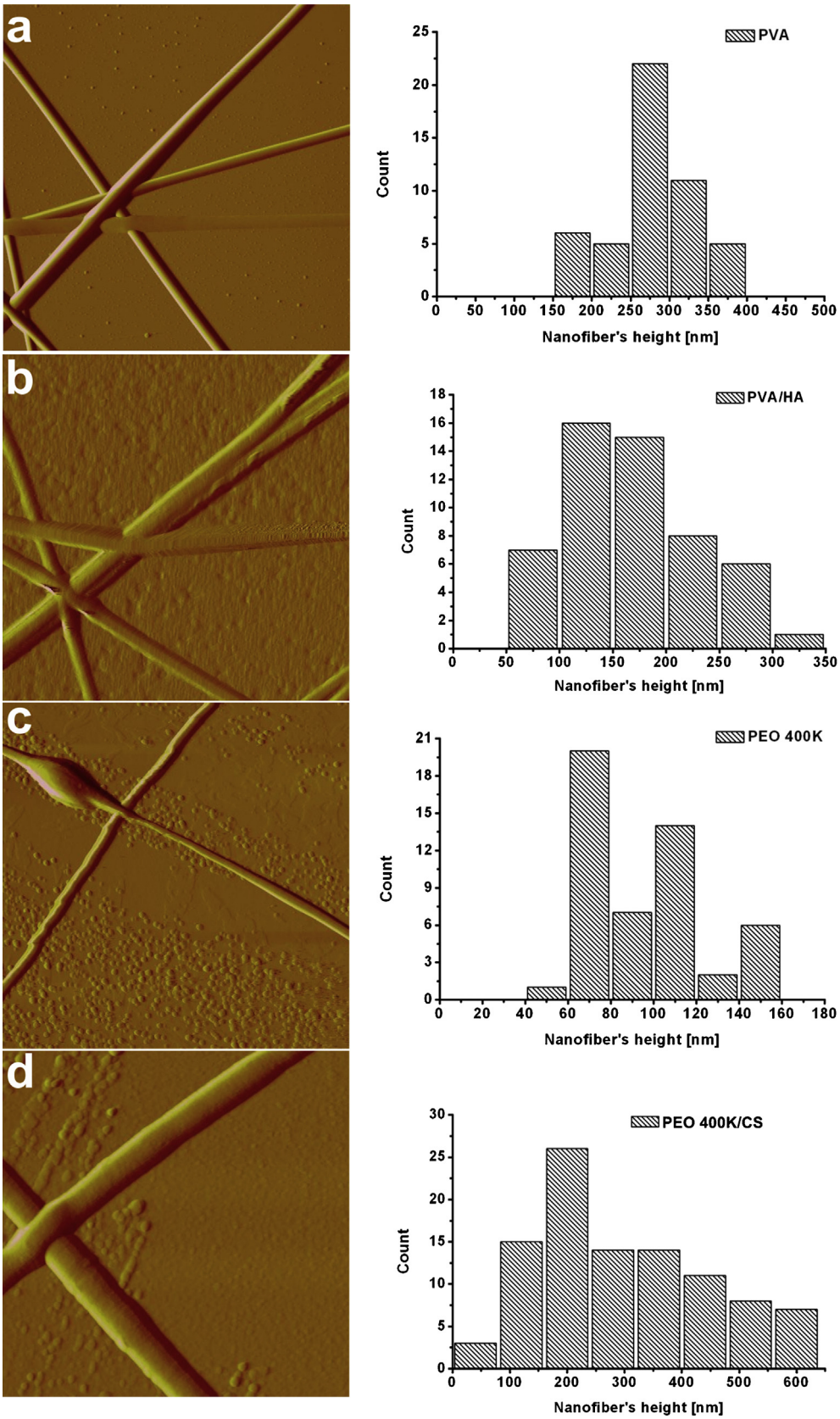

Fig. 4. AFM contact mode images (left) and size distributions (right) of the nanofibers studied: (a) PVA (scan size 15 × 15 μm); (b) PVA/HA (scan size 10 × 10 μm); (c) PEO 400K (scan size 15 × 15 μm); (d) PEO 400K/CS (scan size 10 × 10 μm).

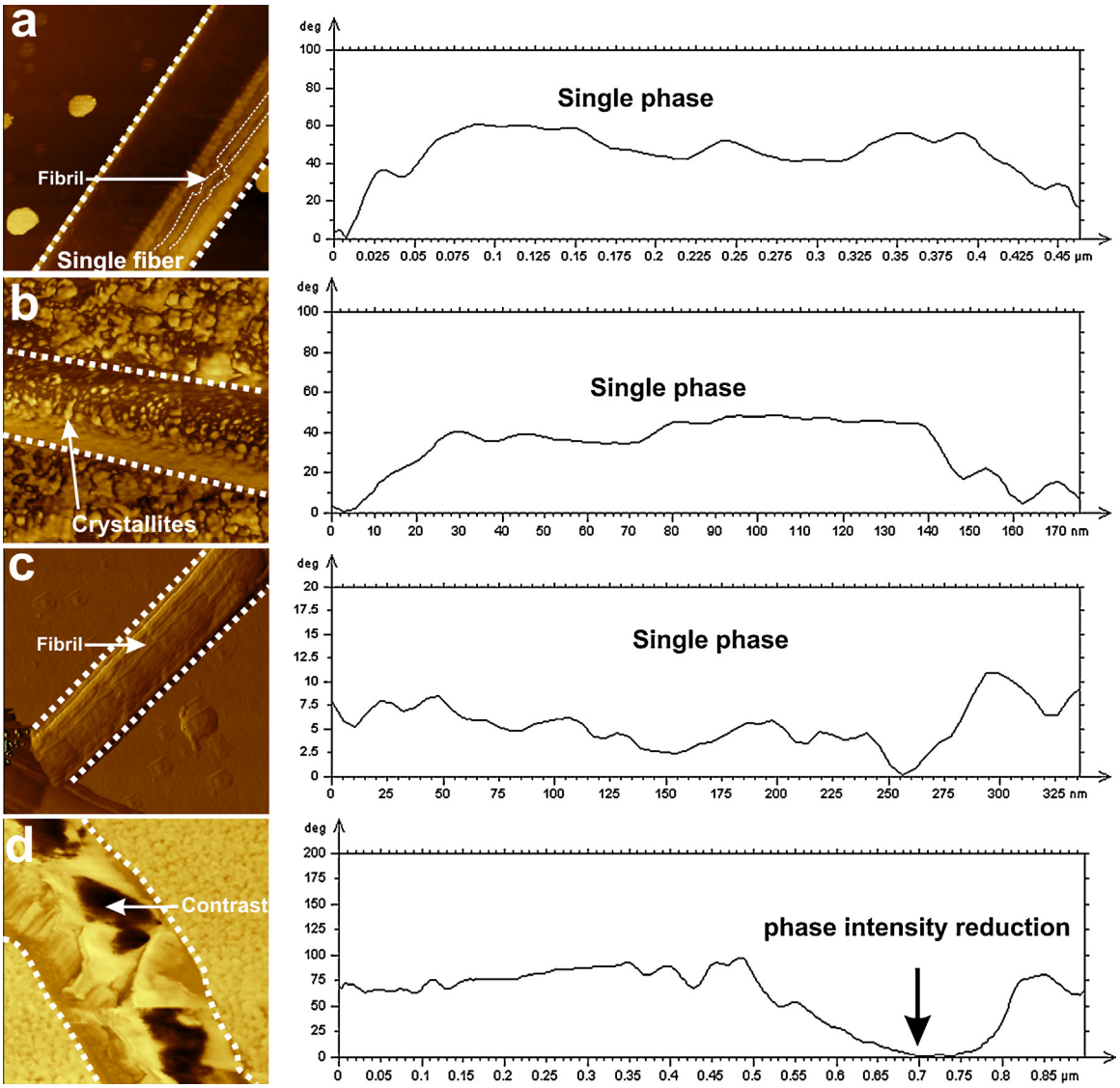

Fig. 5. AFM phase images and phase intensity plots (phase degree vs. cross section length – right panels) of the nanofibers studied: (a) PVA; (b) PVA/HA; (c) PEO 400K; (d) PEO 400K/CS. Dot lines represent the contours of the single nanofibers.

between the AFM tip and the sample. The larger phase in intensity plots (Fig. 5, right side "phase degree *vs.* cross section") is characteristic for harder materials (Magonov and Reneker, 1997).

Accordingly, the ranking of increasing stiffness of the nanofibers studied can be listed: PEO 400K, PVA/HA ≈ PVA, PEO 400K/CS. In order to confirm the reliability of the purposed order, a three-point beam bending test on AFM was performed.

3.5. Mechanical properties of polymeric nanofibers and cast films

A summary of the results obtained on several single nanofibers studied and the calculated bending modulus using Eq. (1) is represented in Fig. 6.

In these classes of polymeric nanofibers, there is a general trend of decrease in the measured bending E with increasing nanofiber height. In some cases, the mechanical properties of the samples studied vary sharply when the object scale drops below a critical threshold (*e.g.*, fiber height).

When the scale of the PEO 400K/CS nanofibers decreased to 240 nm (Fig. 6d) the bending E were no longer the same as the bulk materials (polymeric films; Table 3). Alternatively, it progressively increases with the reduced size of the fibers, representing a "size-dependant" surface effect. Furthermore, the bending E of PVA nanofibers was in a range from 1 to 5.7 GPa, which corresponded to the elastic modulus of PVA films (7.0 ± 0.4 GPa; Table 3) and those reported in the literature (1.9–5.6 GPa) (Lin et al., 2007). Such a result (Fig. 6a) implies that the bending E of the PVA nanofibers is significantly different from the elastic modulus of the PVA cast film (Table 3). In the range from 200 to 300 nm, it is not reasonable to expect a size-dependant surface effect for the PVA nanofibers, which has already been described in the literature. According to the literature data, for PVA nanofibers less than 160 nm, a much more prominent increase in stiffness has been achieved (Tan and Lim, 2006b).

Table 3
Mechanical properties of the polymeric films studied obtained for the nanoindenter.

Polymeric films	Young's modulus (GPa)	Hardness (MPa)
PVA	7.0 ± 0.4	400 ± 40
PVA/HA	3.6 ± 0.3	200 ± 20
PEO 400K	0.8 ± 0.2	30 ± 6
PEO 400K/CS	1.9 ± 0.3	70 ± 20

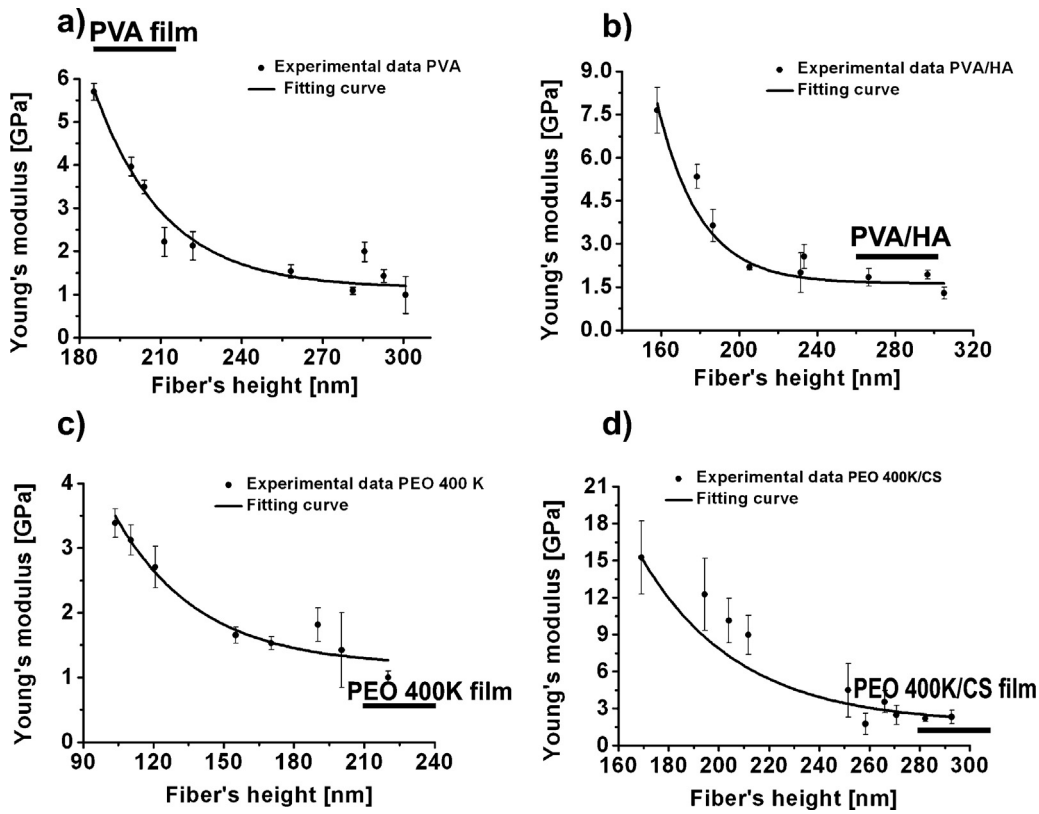

Fig. 6. Young's modulus as a function of nanofiber height.

This result can be explained with mode of the PVA film preparation. Slowly decreasing in solvent content during the preparation of PVA films (solvent casting method) enhanced the progression of crystallization or the lamella growth (crystalline portion). On the other hand, fast evaporation of solvent during the electrospinning induces the formation of amorphous part in greater extent. Eventually, elevation of the crystallinity of PVA polymeric films is the possible reason of larger Young's modulus in comparison to PVA nanofibers.

A physical interpretation of size-dependent nanofiber behavior is still a matter of debate and it has commonly been attributed to the surface tension effect (Dingreville et al., 2005; Cuenot et al., 2004). According to the literature data, a sharp increase in the E of the nano-objects can be described as a sum of the bulk and surface factors (Cuenot et al., 2004, 2000). This approach was established based on the fact that the total energy U of deformed nanofibers includes the surface energy, which is responsible for the increase of E in the range of the small diameters. Therefore, assuming a force F, applied at the beam midpoint and including a deflection δ, the total energy U can be represented as:

$$U = -F\delta + \tfrac{1}{2}K_t\delta^2 + (1-\nu)\gamma\Phi\,\Delta L \quad (8)$$

where K_t is the beam elastic stiffness, Φ is the contour length of its section, ΔL is the length variation, ν is Poisson's ratio, and γ is the surface tension of the material.

The first term in Eq. (8) refers to the work of the applied force, the second one describes the elastic deformation energy of the bent beam, and the third part corresponds to the deformational energy of the surface due to beam extension. Because the last contributes to an increase in the surface, it contributes to the material's compressibility (Arinstein and Zussman, 2011).

From the experimental point of view, the contribution of the surface energy factor is usually neglected because it is related to only a few layers of atoms near the surface, which represent a minor part of the total volume of material of interest. However, due to the enlarged surface-to-volume ratio of the nanofibers, surface effects become more significant and impact parameter in a size-dependent manner (Sharma et al., 2003). Moreover, we suggest that the internal structure has a dominant role in polymer nanofiber reinforcement, which is evident from the AFM measurements (Fig. 6). More precisely, fibers tend to be stiffer only in the direction in which their molecules are oriented. In contrast, fibers are much more elastic if they are bent at right angles to their molecular orientation (Hukins and Meakin, 2000).

The more elastic nature of PVA nanofibers in comparison to PVA/HA can be related to a higher degree of structural order because oriented molecules (Fig. 5d) much more easily slip under applied force. Molecular interactions between the PVA and HA, confirmed with the DSC and ATR measurements, comprised a more compact structure of PVA/HA nanofibers, which resulted in higher bending E.

The absence of ordered thread-like morphology of composite CS nanofibers has as a consequence stiffer structure, which can be confirmed with the largest phase intensity (Fig. 5c). Molecular interactions determined between the CS and PEO 400K (Table 2) is responsible for more compact structure of such nanofibers, which resulted in increasing their rigidity.

From the application perspective, it would be interesting to know whether the nanofibers fulfill the mechanical requirements of the *in vivo* conditions for which they were intended to be implanted. Furthermore, rigid substrates promote cell spread by resisting cell tension, whereas softer substrates contribute to cell differentiation (Saranya et al., 2011; Ingber, 2000).

The results of mechanical properties for the polymeric films demonstrated a positive trend between E and H (Table 3). The film from PEO 400K is the most deformable because it had the lowest E and H in comparison to the stiffest structure of thermally stabilized PVA films.

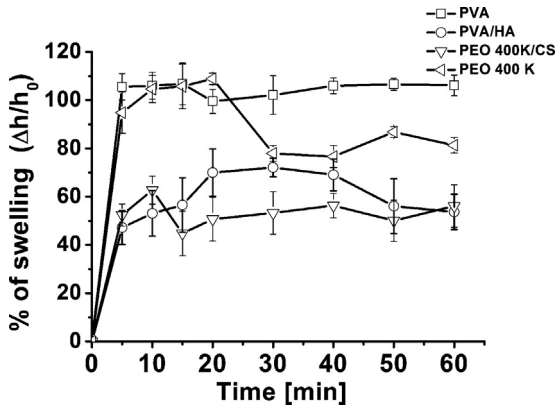

Fig. 7. Swelling degree in water and erosion properties of the nanofibers studied.

According to our results, reinforced nanostructures based on CS (size less than 180 nm) demonstrate a very promising potential in nanomechanical devices for bone–tissue engineering applications because they posses suitable mechanical properties matching those of native bone tissue (Hutmacher et al., 2007). On the other hand, nanofibers based on PVA and PVA/HA are more appropriate for scaffolds for engineering various tissues such as nerves, wounds, skin, and so on (Ingber, 2000).

3.6. Swelling and erosion of the nanofibers studied

Depending upon the application, the physical properties of the nanofibers studied should be investigated, bearing in mind the surrounding environment of the designed scaffold once it is placed in an *in vivo* system. For this reason, we performed the experiments in liquids in order to investigate the swelling behavior of the nanofibers as well as the polymer erosion.

Accordingly, the ranking of swelling degree of the nanofibers studied can be listed: PEO 400K/CS, PVA/HA, PEO 400K, and PVA (Fig. 7). After 60 min of soaking, the fiber structures of PEO 400K/CS and PVA were retained (no erosion). On the other hand, the loss of material though erosion has been determined in the case of PVA/HA and PEO 400K nanofibers. Typical factors that could influence the kinetics of polymeric nanofiber swelling are followed: type of chemical bonds, pH, polymer composition, crystallinity, polymer molecular weight, porosity, and water uptake (Goepferich, 1996). The possible reason for the reduced swelling ratio of PVA/HA in comparison to PVA nanofibers was the intermolecular hydrogen bonding between the carbonyl group of hyaluronic acid and OH group of PVA.

The addition of PEO to CS will reduce the repelling interactions of the CS chains in the solution and thus improve molecular interactions. Confirmed molecular interactions, for composite CS nanofibers, are the possible reason for the smallest swelling ratio and preserved structure during the 60 min of measurement. Our results are in line with the literature data about the excellent integrity of composite PEO/CS nanofibers structure due to its poor solubility in water (Bhattarai et al., 2005, Martinova and Lubasova, 2008). From another perspective, the main measure of the stiffness of an isotropic elastic material, or Young's modulus, is also dependent on the degree of swelling in the given medium (Winter, 1982; Govedarica et al., 2012).

This relationship can be mathematically represented under defined conditions using Eq. (9):

$$E \approx A\left(\frac{V}{V_0}\right)^{-5/3} \tag{9}$$

where E is Young's modulus, V/V_0 is the degree of swelling relative to the initial volume of the polymer (V_0), and A is a constant. Eq. (9) expresses a reciprocal relationship between Young's modulus and the degree of swelling. Accordingly, differences in the % of swelling of the nanofibers studied can be clarified using this expression.

Interpretation of the results is based on average nanofibers height used in the swelling study and their stiffness. According to that, the highest degree of swelling is characteristic for PVA and PEO 400K nanofibers because the lowest bending E was determined. In contrast, the stiffest PEO 400K/CS nanofibers (the largest E) had the most reduced % of swelling.

4. Conclusions

In summary, we introduced the AFM to reveal the morphology, nanomechanical properties, and swelling behavior of single-material (PVA, PEO 400K) and composite nanofibers (PVA/HA and PEO 400K/CS). The mechanical property, namely the bending E, increases as the diameter of the fibers decreases from the bulk down to the nanometer regime (less than 200 nm). The ranking of increasing stiffness according to the AFM measurements of the phase intensity and three-point beam bending test are in agreement, and can be ranked: PEO 400K < PVA/HA ≈ PVA < PEO 400K/CS.

According to our results, composite CS/PEO nanofibers are the stiffest and the most resilient to erosion in an aqueous medium. Consequently, they possess the most appropriate attributes for bone, tendon, and cartilage tissue scaffold engineering. PVA, PVA/HA and PEO nanofibers are more elastic (a smaller bending Young's modulus) and therefore are the most suitable for skin and wound tissue scaffolds. Such elastic nanofibers will also promote cell differentiation, which is essential for the tissue regeneration process.

Acknowledgement

The authors are grateful to the Slovenian Research Agency for financial support for this research: P1-0189, J1-4236, 1000-09-310085, and 1000-11-310213.

Appendix A. Supplementary data

Supplementary data associated with this article can be found, in the online version, at http://dx.doi.org/10.1016/j.ijpharm.2013.06.083.

References

Arinstein, A., Zussman, E., 2011. Electrospun polymer nanofibers: mechanical and thermodynamic perspectives. J. Polym. Sci. B 49, 691–707.
Bhattarai, N., Edmondson, D., Veiseh, O., Matsenb, F.A., Zhang, M., 2005. Electrospun chitosan-based nanofibers and their cellular compatibility. Biomaterials 26, 6176–6184.
Buchko, C.J., Chen, L.C., Shen, Y., Martin, D.C., 1999. Processing and microstructural characterization of porous biocompatible protein polymer thin films. Polymer 40, 7397–7407.
Cuenot, S., Demoustier-Champagne, S., Nysten, B., 2000. Elastic modulus of polypyrrole nanotubes. Phys. Rev. Lett. 85, 1690–1693.
Cuenot, S., Fretigny, C., Demoustier-Champagne, S., Nysten, B., 2004. Surface tension effect on the mechanical properties of nanomaterials measured by atomic force microscopy. Phys. Rev. B, 1–5.
Dingreville, R., Qu, J.M., Cherkaoui, M.J., 2005. Surface free energy and its effect on the elastic behaviour of nano-sized particles, wire sand films. Mech. Phys. Solids 53, 1827–1854.
Du, F., Zhao, W., Zhang, M., Mao, H., Kong, D., Yang, J., 2011. The synergistic effect of aligned nanofibers and hyaluronic acid modification on endothelial cell behaviour for vascular tissue engineering. J. Nanosci. Nanotechnol. 11, 6718–6725.
Fleming, R.G., Murphy, C.J., Abrams, G.A., Goodman, S.L., Nealey, P.F., 1999. Effects of synthetic micro- and nano-structured surfaces on cell behaviour. Biomaterials 20, 573–588.

Fu, Q.Y., Jin, X., Song, J., Gao, X., Han, X., Jiang, Q., Zhao, D., 2010. Size-dependent mechanical properties of PVA nanofibers reduced via air plasma treatment. Nanotechnology 21, 1–5.
Garg, K., Bowlin, G.L., 2011. Electrospinning jets and nanofibrous structures. Biomicrofluidics 5, 013403.
Goepferich, A., 1996. Mechanisms of polymer degradation and erosion. Biomaterials 17, 103–114.
Govedarica, B., Sovány, T., Pintye-Hódi, K., Škarabot, M., Baumgartner, S., Muševič, I., Srčič, S., 2012. Addressing potent single molecule AFM study in prediction of swelling and dissolution rate in polymer matrix tablets. Eur. J. Pharm. Biopharm. 80, 217–225.
Hukins, D.W., Meakin, J.R., 2000. Relationship between structure and mechanical function of the tissues of the intervertebral joint. Am. Zool. 40, 42–52.
Humar, M., Arčon, D., Umek, P., Škarabot, M., Muševič, I., Bregar, B., 2006. Mechanical properties of titania-derived nanoribbons. Nanotechnology 17, 3869–3872.
Hutmacher, D.W., Schantz, J.T., Lam, C.X., Tan, K.C., Lim, T.C., 2007. State of art and future directions of scaffold-based bone engineering from a biomaterials perspective. J. Tissue Eng. Regener. Med. 1, 245–260.
Inai, R., Kotaki, M., Ramakrishna, S., 2005. Structure and properties of electrospun PLLA single nanofibers. Nanotechnology 16, 208–213.
Ingber, D.E., 2000. In: Lanza, R.P., Langer, R., Vacanti, J. (Eds.), Principles of Tissue Engineering. Academic, San Diego, CA, pp. 101–110.
Ji, J., Bar-On, B., Wagner, D., 2012. Mechanics of electrospun collagen and hydroxyapatite/collagen nanofibers. J. Mech. Behav. Biomed. Mater. 13, 185–193.
Jin, L., Wang, T., Zhu, M., Leach, M.K., Naim, Y.I., Corey, J.M., Feng, Z., Jiang, Q., 2012. Electrospun fibers and tissue engineering. J. Biomed. Nanotechnol. 8, 1–9.
Johnson, J., Ghosh, A., Lannutti, J., 2007. Microstructure–property relationships in a tissue-engineering scaffold. J. Appl. Polym. Sci. 104, 2919–2927.
Kim, K., Akada, Y., Kai, W., Kim, B., Kim, I., 2011. Cell attachment property of PVA hydrogel nanofibers incorporating hyaluronic acid for tissue engineering. J. Biomater. Nanobiotechnol. 2, 353–360.
Li, M., Mondrinos, M.J., Gandhi, M.R., Ko, F.K., Weiss, A.S., Lelkes, P.I., 2005. Electrospun protein fibers as matrices for tissue engineering. Biomaterials 26, 5999–6008.
Lin, D.C., Dimitriadis, E.K., Horkay, F., 2007. Elasticity of rubber-like materials measured by AFM nanoindentation. Polym. Lett. 9, 576–584.
Magonov, S.N., Reneker, D.H., 1997. Characterization of polymer surfaces with atomic force microscopy. Annu. Rev. Mater. Sci. 27, 175–222.
Martins, A.M., Alves, C.M., Kasper, F.K., Mikos, A.G., Reis, R.L., 2010. Responsive and in-situ-forming chitosan scaffolds for bone tissue engineering applications: an overview of the last decade. J. Mater. Chem. 20, 1638–1645.
Martinova, L., Lubasova, D., 2008. Electrospun chitosan based nanofibers. Res. J. Text. Application 12, 72–79.
Oliver, W.C., Pharr, G.M., 2004. Measurement of hardness and elastic modulus by instrumented nanoindentation: advances in understanding and refinements of methodology. J. Mater. Res. 19, 3–20.
Pelipenko, J., Kocbek, P., Govedarica, B., Rosic, R., Baumgartner, S., Kristl, J., 2013. The topography of electrospun nanofibers and its impact on the growth and mobility of keratinocytes. Eur. J. Pharm. Biopharm., http://dx.doi.org/10.1016/j.ejpb.2012.09.009.
Peresin, M., Habbibi, Y., Zoppe, J., Pawlak, J., Rojas, O., 2010. Nanofiber composites of polyvinyl alcohol and cellulose nanocrystals: manufacture and characterization. Biomacromolecules 11, 674–681.
Rim, N.G., Shin, C.S., Shin, H., 2013. Current approaches to electrospun nanofibers for tissue engineering. Biomed. Mater. 8, 1–14.
Rošic, R., Kocbek, P., Baumgartner, S., Kristl, J., 2011. Electro-spun hydroxyethylcellulose nanofibers: the relationship between structure and process. J. Drug Deliv. Sci. Technol. 21., 229–236.
Rošic, R., Pelipenko, J., Kristl, J., Kocbek, P., Bešter-Rogač, M., Baumgartner, S., 2013. Physical characteristics of poly (vinylalchohol) solutions in relation to electrospun nanofiber formation. Eur. Polym. J. 49, 290–298.
Rošic, R., Pelipenko, J., Kocbek, P., Baumgartner, S., Bešter-Rogač, M., Kristl, J., 2012. The role of rheology of polymer solution in predicting nanofiber formation by electrospinning. Eur. Polym. J. 48, 1374–1384.
Salvetat, J.P., Briggs, G.A.D., Bonard, J.M., Bacsa, R.R., Kulik, A.J., Stockli, T., Burham, N.A., Forro, L., 1999. Elastic and shear moduli of single-walled carbon nanotube ropes. Phys. Rev. Lett. 82, 944–947.
Saranya, N., Saravanan, S., Moorthi, A., Ramyakrishna, B., Selvamurugan, N., 2011. Enhanced osteoblast adhesion on polymeric nano-scaffolds for bone tissue engineering. J. Biomed. Nanotechnol. 7, 238–244.
Sharma, P., Ganti, S., Bhate, N., 2003. Effect of surfaces on the size-dependent elastic state of nano-inhomogeneities. Appl. Phys. Lett. 82, 535–537.
Stitzel, J.D., Pawlowski, K.J., Wnek, G.E., Simpson, D.G., Bowlin, G.L., 2001. Arterial smooth muscle cell proliferation on a novel biomimicking, biodegradable vascular graft scaffold. J. Biomater. Appl. 16, 22–33.
Subramanian, A., Vu, D., Larsen, G., Lin, H.Y., 2005. Preparation and evaluation of electrospun chitosan-PEO fibers, for potential applications in cartilage tissue engineering. J. Biomater. Sci. Polym. Ed. 16, 861–873.
Tan, E.P.S., Lim, C.T., 2006a. Characterization of bulk properties of nanofibrous scaffolds from nanomechanical properties of single nanofibers. J. Biomed. Mater. Res. 77, 526–533.
Tan, E.P.S., Lim, C.T., 2006b. Effect of annealing on the structural and mechanical properties of electrospun polymeric nanofibers. Nanotechnology 17, 249–265.
Winter, W., 1982. Polysaccharide structure by X-ray fiber diffraction. Methods Enzymol. 83, 87–104.
Yim, E.K.F., Leong, K.W., 2005. Significance of synthetic nanostructures in dictating cellular response. Nanomed. Nanotechnol. Biomed. 1, 10–21.
Zhang, Y.Z., Su, B., Ramakrishna, S., Lim, C.T., 2008. Chitosan nanofibers from an easily electrospinnable UHMW PEO-doped chitosan solution system. Biomacromolecules 9, 136–141.
Zussman, E., Rittel, D., Yarin, A.L., 2003. Failure modes of electrospun nanofibers. Appl. Phys. Lett. 82, 3958–3960.